Crystal growth and thermoelectric properties of CaMn$_{0.98}$Nb$_{0.02}$O$_{3-\delta}$

D.S. Alfaruq [a], M.H. Aguirre [a], E.H. Otal [a,c], S. Populoh [a], L. Karvonen [a], S. Yoon [a], Y. Lu [a], G. Deng [b], S.G. Ebbinghaus [d], A. Weidenkaff [a,*]

[a] Empa, Solid State Chemistry and Catalysis, Ueberlandstrasse 129, CH-8600 Duebendorf, Switzerland
[b] Paul Scherrer Institut, Solid State Chemistry-Laboratory for Development and Methods, Villigen PSI, CH-5232 Switzerland
[c] UTN—Facultad Regional Santa Cruz, Av. Inmigrantes 555, Río Gallegos 9400, Santa Cruz, Argentina
[d] Martin-Luther-Universität Halle-Wittenberg, Institut für Chemie, Kurt-Mothes-Straße 2, D-06120 Halle (Saale), Germany

ABSTRACT

Thermoelectric CaMn$_{0.98}$Nb$_{0.02}$O$_{3-\delta}$ single crystals were grown from sintered polycrystalline material using the traveling-solvent floating zone (TSFZ) method. The floating-zone furnace was operated at over-pressure using an Ar/O$_2$ mixture to prevent evaporation during the growth process. Six twin-domain variants were detected with single-crystal X-ray diffraction (XRD) and confirmed by electron diffraction (ED) and high-resolution transmission electron microscopy (HRTEM). The Seebeck coefficient (S) of the single-crystalline material indicates n-type semiconducting behavior. Within 10 K $< T <$ 125 K a negative peak in S is observed, known to be characteristic of antiferromagnetic ordering. The ferromagnetic long-range ordering, expected on the basis of double exchange between Mn^{4+} and doped Mn^{3+} species, thus appears to remain suppressed in the single-crystalline material.

© 2013 Elsevier B.V. All rights reserved.

1. Introduction

The flexibility of the perovskite structure allows the usage of a wide range of elements, enabling the design of materials with attractive physical and chemical properties [1,2]. Perovskite-type manganates, in particular, have been intensively studied in recent years with regard to colossal magneto resistance (CMR) and thermoelectricity [3–8]. The electrical transport and magnetic properties of manganates are strongly governed by the mixed valence of manganese (Mn^{3+} and Mn^{4+}), the variable charge and/or orbital ordering and the competition between different magnetic interactions [9,10]. Changing the oxygen content alters the Mn^{3+}/Mn^{4+} ratio resulting in a modification of the physical properties [2].

High temperature applications of thermoelectric generators require the development of temperature stable and cheap ceramic materials. Perovskite-type manganates, titanates and cobaltates are the most promising candidates for this application, since their thermochemical stability is demonstrated and thermoelectric figure of merit (ZT) values of $ZT > 1$ were reached [11,12]. The replacement of Mn in CaMnO$_3$ with higher-valent transition metals leads to materials with interesting properties particularly in the field of thermoelectricity. The substitution of Nb for Mn in

CaMnO$_3$, for instance, produces a semiconducting compound with a large negative Seebeck coefficient (S) making it a promising n-type material for thermoelectric converters. Perovskite-type manganates were applied successfully as n-type legs in thermo-electric oxide modules [13–17] which were used for the demonstration of direct solar energy converters. The reason for the good thermoelectric performance of the Ca-manganates is the formation of a mixed valence where manganese is present in the oxidation states Mn^{4+} and Mn^{3+}, associated with the generation of itinerant electrons increasing the charge carrier concentration. These electrons can easily migrate via the double exchange mechanism, thus, lowering the electrical resistivity compared to insulating non-substituted CaMnO$_3$ [3,18]. The thermoelectric figure of merit ZT is a measure of a material's thermoelectric quality and a function of S, the electrical resistivity (ρ), and the thermal conductivity (κ): $ZT = S^2 T / \rho \kappa$. Previous studies showed that nanostructured polycrystalline CaMn$_{0.98}$Nb$_{0.02}$O$_{3-\delta}$ reaches values of $ZT_{1000\,K} = 0.32$ [3,18] owing to a substantial decrease of the electrical resistivity compared to CaMnO$_3$, while the high absolute value of S and low value of κ remain less influenced by the Nb substitution. Low thermal conductivity was achieved by the formation of a nano twin-domain structure which has to be formed under a controlled way. Single crystals are needed as reference materials without grain boundaries to understand the formation process and influence on thermoelectric properties.

In this study, the CaMn$_{0.98}$Nb$_{0.02}$O$_{3-\delta}$ single crystals were grown from polycrystalline rods using the traveling-solvent floating zone

---

(TSFZ) method. The structure and morphology of the as-crystallized material was characterized using X-ray diffraction (XRD), scanning electron microscopy (SEM), high resolution transmission electron microscopy (HRTEM) and electron diffraction (ED). In addition, the Seebeck coefficient was measured in a wide temperature range.

2. Experimental

Polycrystalline perovskite-type powder with a nominal composition of $CaMn_{0.98}Nb_{0.02}O_{3-\delta}$ was prepared *via* a soft-chemistry synthesis route [18]. The resulting powder was densified, packed into latex tubes and hydrostatically pressed at 400 MPa. High-density green-body rods of 100 mm in length and 8 mm in diameter were obtained and mounted vertically in an aluminum oxide tube. The green-body rods were heated to 1473 K at a rate of 300 K/h and sintered for 15 h for further densification. A density higher than 92% of the theoretical value was achieved. This high density of the sintered rods prevents suction from the liquid zone into the feed rod by capillary forces and inhibits gas bubble formations which can lead to zone instability during the TSFZ crystallization. The sintered rods were re-crystallized into ingots of *approx.* 70 mm in length and 3 mm in diameter by using a four-mirror floating-zone furnace (FZ-T-10000-H-HR-I-VPO-PC, Crystal Systems Corp., Japan) [19,20] with four 300 W halogen lamps as heating sources. The crystallization conditions were adjusted according to previous specifications [22] and the phase diagrams of the Ca–Mn–O [21,23,24] and $CaMn_{1-x}Mo_xO_3$ [9] systems. The homogeneity of the traveling floating zone was maintained by clockwise and counterclockwise rotations (20 rpm) of the feed rod and seed rod, respectively. In order to obtain high-quality single-crystalline material a slow growing rate (4 mm/h) was chosen. An elevated pressure (500 kPa of 20% O_2 in argon; total flow rate of 0.5 L/min) was applied to prevent evaporation of the precursor material during the crystal growth process [21].

The oxygen content of the sintered material and floating-zone-grown crystals was analyzed by thermogravimetric (TG) analysis using a Netzsch STA 409 CD thermobalance. The samples were heated up to 1373 K at a rate of 10 K/min in a 20% H_2–He atmosphere. As confirmed with an XRD measurement under these conditions the sample is reduced according

$$CaMn_{0.98}Nb_{0.02}O_{3-\delta}(s)+(0.97-\delta)\quad H_2\to CaO(s)+0.98\quad MnO(s)+0.01$$
$$Nb_2O_5(s)+(0.97-\delta)\ H_2O\ (g) \tag{1}$$
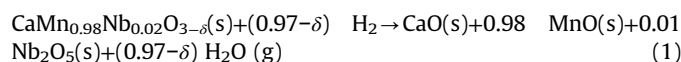
Phase composition and crystallinity of the calcined, sintered and crystallized $CaMn_{0.98}Nb_{0.02}O_{3-\delta}$ materials were checked from their powder XRD patterns collected with a PANalytical X´Pert PRO powder diffractometer (θ–2θ Bragg–Brentano geometry, Cu-K$_{\alpha 1}$ radiation: 1.5406 Å). Specifically, the powder XRD data for the grown crystal was collected from a central piece of the ingot, which was ground to powder prior to the collection. The diffraction patterns were collected in the range of $20° < 2\theta < 100°$ with an angular step interval of $0.0167°$. In the case of the data collected from the ground crystal, a Rietveld analysis using the software Fullprof [25] was performed in order to extract the crystal-lattice parameters, atomic positions and displacement parameters as well as bond-lengths and distances. The Thompson-Cox-Hastings pseudo-Voigt function was chosen to describe the peak shape.

For the single-crystal XRD the floating-zone crystallized ingot was cut transversally into pieces of *approx.* 5 mm in length and 3 mm in diameter at different positions. The crystallographic orientation of the cut pieces were determined with the Laue method. The X-ray reflections were recorded by two CCD cameras (Photonic Science Ltd., U.K.) and the orientation of the crystal was determined from the data using the simulation program Orient Express [26]. The single-crystal X-ray diffraction patterns were recorded using a STOE IPDS-2T imaging-plate diffractometer operating with Mo-K$_\alpha$ radiation. A total set of 240 frames using two different ϕ angles and $\Delta\omega=1°$ was recorded. The distance between imaging plate and sample was set to 45 mm resulting in a maximum 2θ of $75°$. Peak integration and data processing were carried out with the STOE X-Area program suite (Version 1.54) and structure refinement was done with the program ShelXL97 [27].

Electron diffraction (ED) and high resolution transmission electron microscopy (HRTEM) were performed with a JEOL-SEM 2200FS with an in-column filter. The local composition was determined by energy dispersive X-ray analysis (EDX). The texture of the crystallized material was studied with a FEI Nova NanoSEM 230 scanning electron microscope operated in secondary electron (SE) and back-scattered electron (BSE) modes together with EDX analysis to distinguish possible phase segregation. The TEM samples of the crystal were prepared both by a thinning process including mechanical polishing and Ar ion milling to achieve the transparency for TEM analysis, and by suspending fine crushed powder in alcohol. For the SEM analysis, a transversal cut of the ingot (3 mm diameter × 4 mm long) was polished to mirror-like quality by mechanical polishing with diamond papers (15, 9, 6, 3 μm).

The Seebeck coefficient of the floating-zone crystallized material was measured on a bar-shaped specimen (7.5 × 1.6 × 2.82 mm³) in the temperature range of $10\,K < T < 400\,K$ using a Physical Property Measurement System (PPMS) from Quantum Design equipped with the thermal transport option (TTO). The measurement was carried out under vacuum (10^{-5}–10^{-6} mbar). Attempts to measure

Table 1
Refined crystal-structural parameters of the crushed sample from a $CaMn_{0.98}Nb_{0.02}O_{3-\delta}$ single-crystal.

Name		$CaMn_{0.98}Nb_{0.02}O_{3-\delta}$
Diffractometer		PANalytical X´Pert PRO
Radiation source		Lab X-ray Cu$K_{\alpha 1}$
Wavelength (Å)		1.5406
Temperature (K)		298
2θ range (°)		20–100
Space Group		*Pbnm*
a (Å)		5.2744 (1)
b (Å)		5.2924 (1)
c (Å)		7.4692 (1)
V (Å³)		208.4998
Ca	*x*	0.9840 (10)
	y	0.0307 (6)
	z	0.25
	B_{iso} (Å²)	1.05 (6)
	site	4c
	occ.	0.5
Mn/Nb	*x*	0.5
	y	0
	z	0
	B_{iso} (Å²)	0.21 (4)
	site	4b
	occ.	0.49/0.01
O1	*x*	0.0559 (16)
	y	0.4832 (18)
	z	0.25
	B_{iso} (Å²)	1.35 (10)
	site	4c
	occ.	0.5
O2	*x*	0.7048 (13)
	y	0.2802 (16)
	z	0.0325 (11)
	B_{iso} (Å²)	1.35 (10)
	site	8d
	occ.	1.0
R_p		2.15
R_{wp}		2.85
χ^2		2.54

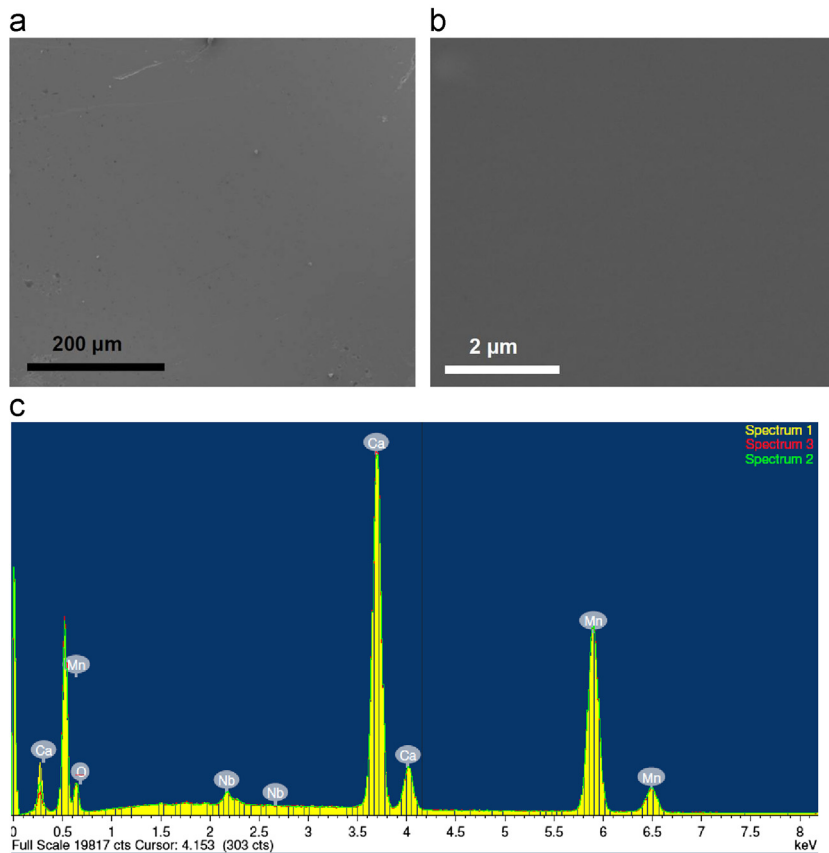**Fig. 1.** SEM images of $CaMn_{0.98}Nb_{0.02}O_{3-\delta}$ using (a) secondary electron (SE) analysis in the central region of the ingot showing the perovskite single phase; (b) BSE analysis showing the central part of the ingot free from secondary phases; and (c) EDX scan of the central part of the ingot.

the electrical resistivity and thermal conductivity of the material were hindered by cracks appearing randomly in the crystal leading to inconsistent results. Efforts to eliminate the cracks by applying slower crystal growth rates (0.3–2.9 mm/h), post-annealing under high pressure (1100 K at 500 kPa) or slow cooling after growing (0.5 to 2 K/h) could not solve the problem. Unlike in the case of the charge carrier transport, porosity or cracks is not expected to have any significant influence on the $S(T)$ behavior [28].

3. Results and discussion

The powder XRD data of the calcined and sintered materials confirmed perovskite-type single phase samples consistent with
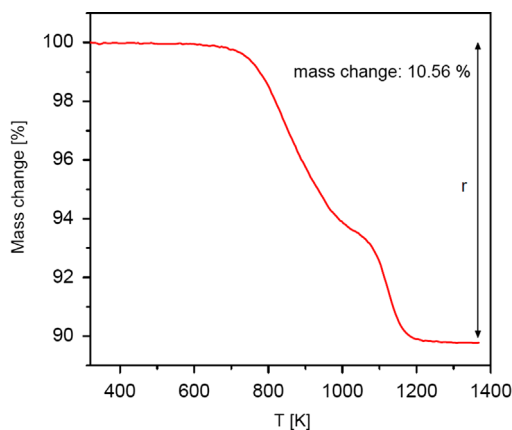

Fig. 2. H_2-reduction (20 % H_2 in He atmosphere) TGA curve of the $CaMn_{0.98}Nb_{0.02}O_{3-\delta}$ crystal.

previous reports [3,18]. The Rietveld refinement results for the powder XRD data recorded from crushed center of the crystal ingot (homogeneous part) confirmed that the main phase of the floating-zone crystallized $CaMn_{0.98}Nb_{0.02}O_{3-\delta}$ has an orthorhombic crystal structure with the space group *Pbnm*. The refined crystal structural parameters are shown in Table 1. Although no

Table 2
Crystal data and structure refinement of the $CaMn_{0.98}Nb_{0.02}O_{3-\delta}$ single crystal.

Diffractometer	STOE IPDS-2T
Temperature (K)	293
Wavelength (Å)	0.71073
Crystal system, space group	Orthorhombic, Pbnm (#62)
Unit cell dimensions (Å)	$a=5.2984(6)$
	$b=5.2984(6)$
	$c=7.4930(8)$
Volume	210.35(4)
Z, Calculated density (g cm^{-3})	4, 4.540
Absorption coefficient (mm^{-1})	8.4
$F(000)$	278
Crystal size (mm^3)	$0.1 \times 0.1 \times 0.1$
Theta range for data collection	3.9–37°
Index ranges	$-8 \leq h \leq +8$
	$-8 \leq k \leq +8$
	$-12 \leq l \leq 12$
Reflections collected/ unique	2962/533
Refinement method	Full-matrix least-squares on F^2
Absorption correction	numerical (6 faces)
Data/ restraints/ parameters	2792/0/34
Goodness-of-fit on F\widehat2	0.957
Final R indices [I > 2sigma(I)]	$R_1=0.0392$, $wR_2=0.1284$[a]
R indices (all data)	$R_1=0.0543$, $wR_2=0.1334$[a]
Extinction coefficient	0.041(5)
Largest diff. peak and hole (eÅ^{-3})	1.41 and -0.96

[a] $w=1/[\sigma^2(F_o^2)+(\ 0.0923\ast P)^2]$ where $P=(F_o^2+2F_c^2)/3$.

$Ca_2Mn_2O_5$ was detectable by SEM–BSE as a secondary phase, it was detected in powder XRD. Quantitative phase analysis (QPA) performed during the Rietveld refinement revealed 8.37% of $Ca_2Mn_2O_5$ as impurity phase.

SEM images of the cut and polished ingot surfaces (with an approximate diameter of 3 mm) are shown in Fig. 1. SEM–SE image of the central region of the ingot (0.6×0.3 mm^2) reveals a dense pore-free morphology (Fig. 1a) with an average composition of $CaMn_{0.975(3)}Nb_{0.025(3)}O_{3-\delta}$ (error estimation of the last decimal given in parentheses), as determined by EDX analysis (Fig. 1c). The SEM–BSE image (Fig. 1b) of the same central part of the ingot as in Fig. 1a verifies a homogeneous chemical composition.

The oxygen stoichiometry was calculated using the relative weight loss (r) measured by TGA in reductive atmosphere. The relation between δ and r (Eq. (2)) can be established based on the stoichiometry of the decomposition reaction Eq. (1):

$$r = \frac{(MCMNO - \delta MO) - (MCaO + (0.975 \pm 0.003)MMnO + (0.025 \pm 0.003)/2MNb_2O_5)}{(MCMNO - \delta MO)},$$
(2)

where Mi = formula weight of the compound i. CMNO = $CaMn_{0.975(3)}Nb_{0.025(3)}O_3$, as defined from the EDX results above.

For the crystals a weight loss r of 10.56(3)% was determined (Fig. 2). A similar result was obtained for the sintered rod material. Using Eq. (2) an oxygen deficiency of $\delta = 0.01(2)$ is calculated suggesting the chemical composition $CaMn_{0.05(1)}^{III}Mn_{0.92(2)}^{IV}Nb_{0.025(3)}^{V}O_{2.99(2)}$. This finding reveals that no significant oxygen deficiencies are present in the crystals. It is worth to mention that the determined oxygen content is an average value from the central part of the ingot.

The Laue pattern recorded revealed a regular distribution of sharp reflections indicating single crystallinity and an [010] crystallographic orientation along the growth axis for the pieces cut from the crystal. This observation was also confirmed by the HRTEM and ED results. The homogeneous perovskite-type phase of a $0.1 \times 0.1 \times 0.1$ mm^3 piece cut from the central part of the ingot was confirmed by single-crystal diffraction and SEM. The indexing of the diffraction pattern indicated a primitive cubic cell with $a_c = 7.4930(8)$ Å. The intensity analysis however showed that the internal R values in both possible cubic Laue classes were unusually high (~0.25). Additionally, the suggested space groups $P2_13$ and $P4_232$ are uncommon for perovskite related oxides. Attempts to find a reference structure in these two space groups were not successful, implying a too high symmetry due to twinning. A peak intensity analysis revealed a set of reflections with particularly high intensities. This subset could be indexed using a (pseudo-)tetragonal primitive cell with $a = b = a_c/\sqrt{2}$ and $c = a_c$. The observed extinctions suggest the possible orthorhombic space group $Pbnm$ (non-standard setting of $Pnma$) which is in agreement with the Rietveld refinement of the powder XRD patterns and widely accepted for calcium manganese oxide (ICSD Collection Code: 082211) [29]. In fact, the structural refinement in this space group immediately led to reasonable results. The inclusion of a second twin domain according to the transformation matrix

$$\begin{pmatrix} 0 & 1 & 0 \\ 1 & 0 & 0 \\ 0 & 0 & -1 \end{pmatrix}$$
(1)

resulted in already acceptable residual parameters of $R_1 = 0.037$ and $wR_2 = 0.087$. On the other hand, the presence of a second set of weaker reflections clearly indicates that a more complex twinning had to be taken into account. This problem has already been discussed for Ca-substituted $LaMnO_3$ by Van Aken et al. [30]. The key idea of the twinning model is that the long axis of the orthorhombic perovskite structure can be oriented along any of the three orthogonal axes, in turn giving rise to the apparent cubic cell symmetry. For any of these three orientations two twin domains exist, which are correlated by an exchange of a and b and the inversion of c according to (1) (correspondingly, an exchange of a and c and the inversion of b for the $Pnma$ space group). This results in a six-fold twin, leading to a strong overlap of the signals from the different domains. Since we chose to use the non-standard space group $Pbnm$, the resulting transformation matrices for the axes and hkl-values differ from those in [26] and are therefore listed below:

$$M1 = \begin{pmatrix} -1/2 & 0 & 1/2 \\ 1/2 & 0 & 1/2 \\ 0 & 1 & 0 \end{pmatrix} \quad M2 = \begin{pmatrix} 1/2 & 0 & 1/2 \\ -1/2 & 0 & 1/2 \\ 0 & -1 & 0 \end{pmatrix}$$

$$M3 = \begin{pmatrix} 0 & 1/2 & -1/2 \\ 0 & 1/2 & 1/2 \\ 1 & 0 & 0 \end{pmatrix} \quad M4 = \begin{pmatrix} 0 & 1/2 & 1/2 \\ 0 & 1/2 & -1/2 \\ -1 & 0 & 0 \end{pmatrix}$$

$$M5 = \begin{pmatrix} 1/2 & 1/2 & 0 \\ -1/2 & 1/2 & 0 \\ 0 & 0 & 1 \end{pmatrix} \quad M6 = \begin{pmatrix} -1/2 & 1/2 & 0 \\ 1/2 & 1/2 & 0 \\ 0 & 0 & -1 \end{pmatrix} \quad (2)$$

A program was written that reads these transformation matrices and generates the corresponding intensity file in the ShelXL HKLF 5 format. Data assessments showed that there are sets of signals with the contributions of all six twin domains, while there are other signals with contributions of four or only two

Table 3
Atomic coordinates and equivalent isotropic displacement parameters of $CaMn_{0.98}Nb_{0.02}O_{3-\delta}$ single crystal. U_{eq} is defined as one third of the trace of the orthogonalized U_{ij} tensor.

Atom	x	y	z	SOF	U_{eq} [Å^2]
Ca	−0.00572(8)	0.53197(11)	0.75	0.5	0.0070(1)
Mn/Nb	0	0	0.5	0.49/0.01	0.0021(1)
O1	0.06660(33)	−0.01370(25)	0.75	0.5	0.0044(3)
O2	−0.28763(21)	−0.21353(22)	0.53342(17)	1.0	0.0074(2)

Table 4
Anisotropic displacement parameters (Å^2) of $CaMn_{0.98}Nb_{0.02}O_{3-\delta}$ single crystal.

Atom	U_{11}	U_{22}	U_{33}	U_{23}	U_{13}	U_{12}
Ca	0.0044(2)	0.0088(2)	0.0077(2)	0	0	−0.0011(1)
Mn/Nb	0.0020(2)	0.0016(2)	0.0025(2)	0.0005(5)	0.0001(1)	−0.0001(1)
O1	0.0055(7)	0.0041(6)	0.0037(6)	0	0	0.0003(4)
O2	0.0055(4)	0.0066(4)	0.0101(4)	0.0001(4)	0.0016(4)	−0.0026(3)

Table 5
Selected inter-atomic distances (Å) and bond angles (°) in $CaMn_{0.98}Nb_{0.02}O_{3-\delta}$ single crystal.

Name		$CaMn_{0.98}Nb_{0.02}O_{3-\delta}$
Distance		
Mn/Nb–O1	x2	1.9059(11)
Mn/Nb–O2	x2	1.9076(4)
Mn/Nb–O3	x2	1.9145(11)
Ca–O1		2.3392(18)
Ca–O1		2.4376(15)
Ca–O1		2.9164(15)
Ca–O1		2.9815(18)
Ca–O2	x2	2.3504(13)
Ca–O2	x2	2.5851(13)
Ca–O2	x2	2.6021(13)
Angle		
Mn/Nb–O1–Mn/Nb		158.23(10)
Mn/Nb–O2–Mn/Nb		157.43(7)

domains. This partial merohedral twin structure allows determination of the fractions of the individual twin domains. During refinement it turned out that the two twin domains corresponding to the above-mentioned matrices M5 and M6 contribute only about 1.5% and 2.5%, respectively, to the signals. Therefore, these domains were disregarded in the final runs. Since the Nb content in the crystals is very small ($n(Nb)/n(Mn)=0.026(3)$), no attempts were made to refine the Mn/Nb site occupation. Instead, all positions were refined using the nominal composition $CaMn_{0.98}Nb_{0.02}O_3$. The obtained R_1 values of 0.039 for reflections with $I>2\sigma$ and 0.054 for all reflections are in the expected range
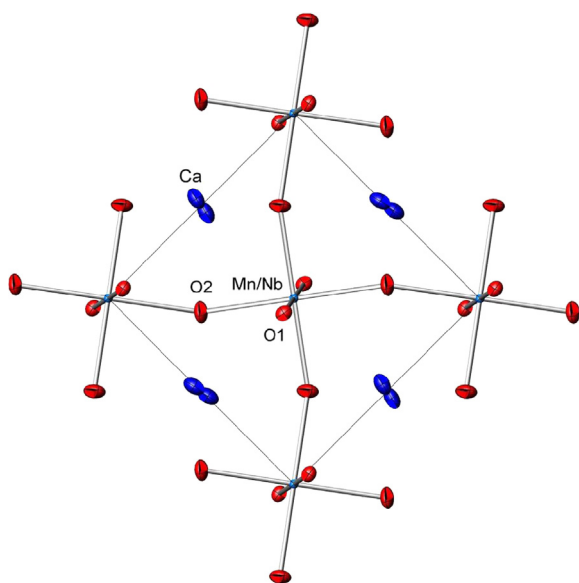
Fig. 3. Crystal structure of $CaMn_{0.98}Nb_{0.02}O_{3-\delta}$ viewed along c axis based on the crystal refinement parameters. Anisotropic displacement parameters are shown with 90% probability.

proving the applied structural model correct. The rather large wR_2 values given in Table 2 are due to a different data handling in ShelXL of files with HKLF 4 and HKLF 5 format. In HKLF 4 files all equivalent reflections are merged, which does not apply for HKLF 5 files. This results in much higher R_1 and wR_2 values as can easily be verified by adding the code MERG 0 in any ShelXL instruction file.

The results of the structure refinement are listed in Tables 3 and 4. Selected bond lengths and angles are specified in Table 5. Fig. 3 shows a representation of the crystal structure viewed along the **c** axis (in *Pbnm* setting). Anisotropic displacement parameters are depicted with a 90% probability. Analysis of the Mn/Nb–O bond lengths reveals a nearly-tetragonal site symmetry with two bonds being significantly longer (≈ 0.008 Å) than the other four which is expected for the Jahn–Teller active Mn^{3+} ion. However, the Jahn–Teller elongation is not very pronounced since the Nb^{5+} content and therefore also the amount of Mn^{3+} is small (based on the oxygen content ($3-\delta$) determined by TGA).

It should be noted that almost identical results for atomic positions, displacement parameters and in turn bond lengths and angles were obtained from the refinement of the reduced dataset described above. This proves the approach of six twin domains correct. The crystal was re-measured at 160 K to check for possible phase transitions. It was found that the crystal structure remains basically identical with the apparent cubic cell parameter being slightly shorter ($a_c \approx c = 7.4852(6)$). Especially, no splitting of the diffraction peaks was observed, i.e. the relation $a \approx b \approx c/\sqrt{2}$ is preserved at low temperatures. The Mn/Nb–O bond lengths (Mn/Nb–O1: 1.9053 (3) Å, Mn/Nb–O2: 1.9054(7) Å, Mn/Nb–O2: 1.9142 (7) Å) and angles (Mn/Nb–O1–Mn/Nb: 158.33(7)°, Mn/Nb–O2–Mn/Nb: 156.96(5)°) are only slightly modified. Since no prominent changes in the structural parameters were observed, details of the low temperature results are not listed here.

Fig. 4 shows HRTEM micrographs of single-domain perovskite with zone axis: (a) [001], (b) [100], and (c) [110] in *Pbnm* setting ($a \approx b \approx a_p\sqrt{2}$, $c \approx 2a_p$). The presence of twin domains detected by single-crystal XRD
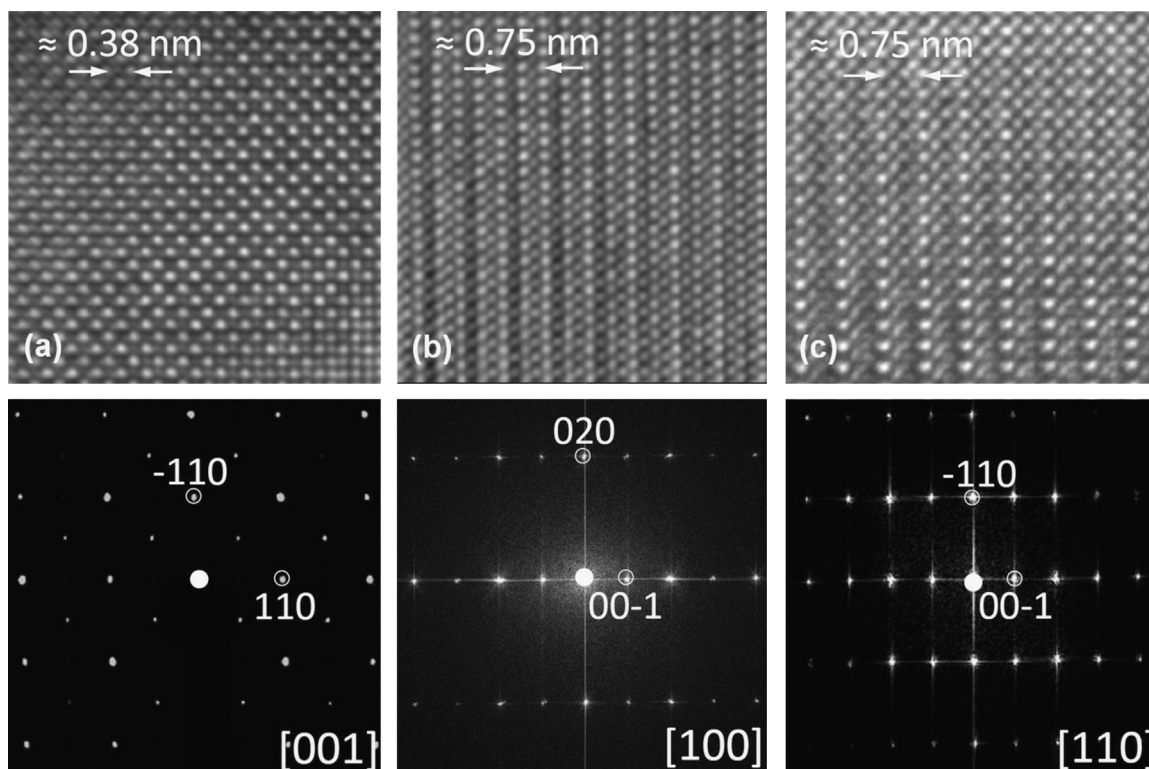

Fig. 4. HRTEM image and respective FFT images of single-domain perovskite with zone axis: (a) [001], (b) [100], and (c) [110] in *Pbnm* setting ($a \approx b \approx a_p\sqrt{2}$, $c \approx 2a_p$).

was confirmed by HRTEM and ED. Fig. 5 shows typical twin-domain boundaries. In part A, the $\hat{c}$ axes of the two observed twin domains, (1) [−110] and (2) [110], are both plane- and mutually perpendicular. In part B, the $\hat{c}$ axis of domain (2) [110] is plane parallel and that of domain (3) [001] is plane perpendicular, while mutually perpendicular to each other. These combinations of twin domains result in a permutation of the $\hat{c}$ axis in two (1+2=A, 2+3=B) or three directions (A+B=C) in 3D-space as described by single-crystal diffraction analysis with the matrices M1–M6 and demonstrated by using FFT and ED patterns Fig. 5 (bottom row). Another frequent combination of twin domains is [100] and [010] (not shown).

The existence of layered oxygen-vacancy planes arranged into a brownmillerite-like configuration and intergrown in diverse orientations within the main phase with disordered oxygen vacancies was revealed from several crushed single-crystal particles by using HRTEM. Fig. 6 shows the [101] zone axis HRTEM image of $CaMn_{0.98}Nb_{0.02}O_{3-\delta}$, where the direction [010] presents an intergrowth superstructure diffraction corresponding to $(\sqrt{2} \times 4\sqrt{2})\, a_p$ R45° oxygen vacancy order. As described in detail in [31], such a vacancy ordering scheme creates

an ED pattern with extra diffraction spots in (1/4, k, l), indicating a superstructure with a $A_nM_nO_{3n-1}$ ($n=4$) stoichiometry and consisting of $(n-1)$ perovskite-like layers of MO_6 octahedra separated by a single layer of MO_4 tetrahedra.

Fig. 7 shows the temperature dependence of the Seebeck coefficient (S) of the single-crystalline $CaMn_{0.98}Nb_{0.02}O_{3-\delta}$ in the temperature range of 10 K < T < 400 K. The value of S remains negative over the entire covered temperature range, indicating n-type conductivity. Heikes formula generally is not applicable in the measured temperature range, as the high-temperature region signaled by a constant S is not yet reached [32–35]. The low-temperature range features a peak in S with $(-S)_{max} = 197\ \mu V/K$ at $T=42\ K$ followed by $(-S)_{min} = 95\ \mu V/K$ at $T=125\ K$. Based on earlier studies [4,36,37], this phenomenon indicates a charge localization due to antiferromagnetic ordering, which outweighs the ferromagnetic interactions—otherwise expected, because of the double exchange between the Mn^{4+} host species and the electron-doping induced Mn^{3+} guest species [4,36]. At the paramagnetic temperature range of the measurement (125 K < T < 400 K) a linear increase of −S occurs, in accordance with
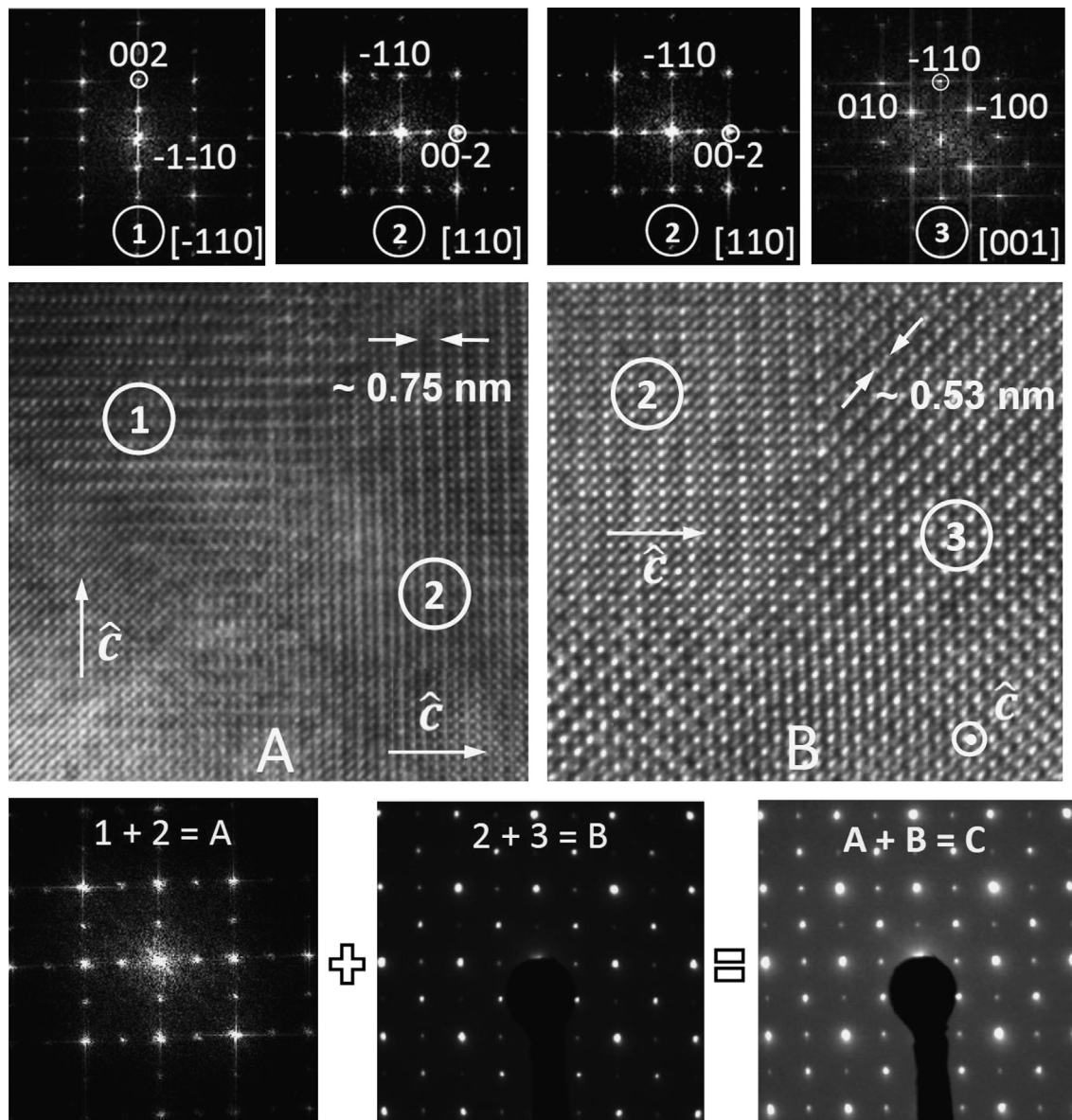

Fig. 5. (Middle row) HRTEM images showing (A) a boundary of (1) [−110] and (2) [110] twin domains and (B) a boundary of (3) [110] and (4) [001] twin domains. (top row) FFT converted images of the domains (1) to (4) in HRTEM images to illustrate the expected ED patterns. (bottom row) The ED pattern (A+B=C) is explainable through combining the superpositional FFT patterns of the regions (1+2=A) and (2+3=B), which indicates a permutation of the $\hat{c}$ in the three directions of space.
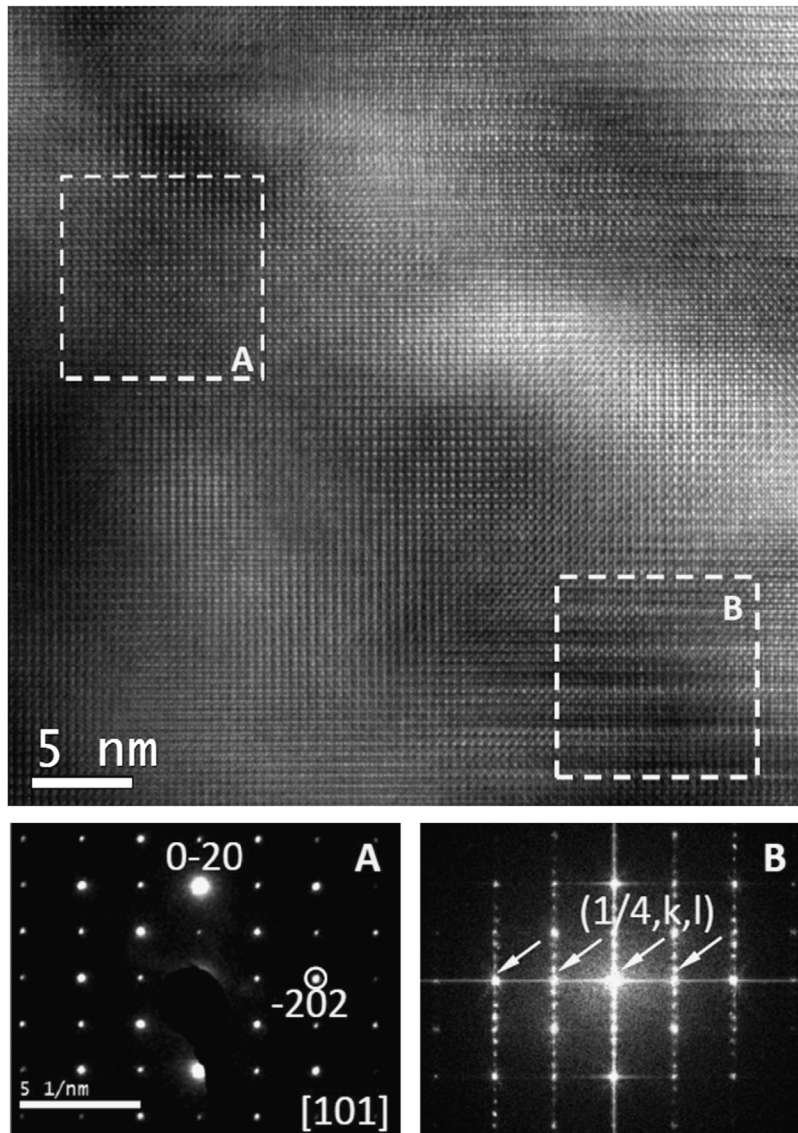
Fig. 6. (Upper row) HRTEM image of $CaMn_{0.98}Nb_{0.02}O_{3-\delta}$ along the [101] zone axis (A) with an intergrowth of $Ca_2(Mn,Nb)_2O_5$ (B) with oxygen vacancy order giving rise to a superstructure $(\sqrt{2} \times 4\sqrt{2}) a_p$ R45°. (Bottom row) FFT images of the domains (A) and (B).

a proposed single-band metal interpretation assuming high charge carrier mobility and high density of states at the Fermi level (E_F), the latter provided by a narrow e_g band [6]. The observed behavior is in line with former results on electron-doped calcium-manganese-oxide perovskites [36–38]. Interestingly, in our previous study [37] it was pointed out that the appearance of the $(-S)_{max}$ and preference of antiferromagnetic over ferromagnetic interaction depends on the synthesis approach. This might be related to the distribution degree of the Mn^{3+} species in the Nb-for-Mn substituted $CaMnO_{3-\delta}$ matrix and of the resulting ferromagnetic clusters. Highly homogeneous distribution, expected after floating-zone melting, possibly disables the long-range coupling.

4. Conclusion

Thermoelectric $CaMn_{0.98}Nb_{0.02}O_{3-\delta}$ crystals were successfully grown from polycrystalline rods applying the TSFZ method. Both the polycrystalline and the floating-zone crystallized materials have an orthorhombic crystal structure with *Pbnm* space group. The floating-zone crystallized material was found to feature large single-crystalline domains. Six twin-domain variants were detected in the single crystal by single-crystal XRD and ED-HRTEM studies, out of which four (M1 to M4) were found to be the more commonly existing orientations in the measured crystal. Twin-domains are beneficial for high *ZT* values, because phonon transport is hindered while electron transport is not diminished. The Seebeck coefficient (*S*) of the single-crystalline material indicates *n*-type semiconducting behavior and is identical with literature data of polycrystalline samples of the same composition [18]. Within $10\,K < T < 125\,K$ a negative peak in *S* is observed, known to be characteristic of antiferromagnetic ordering. The ferromagnetic long-range ordering, expected on the basis of double exchange between Mn^{4+} and doping-induced Mn^{3+} species, remains suppressed in the single-crystalline material, possibly because of a homogeneous distribution of the Nb^{5+} substituents and the induced Mn^{3+} species, disabling long-range ferromagnetic ordering.
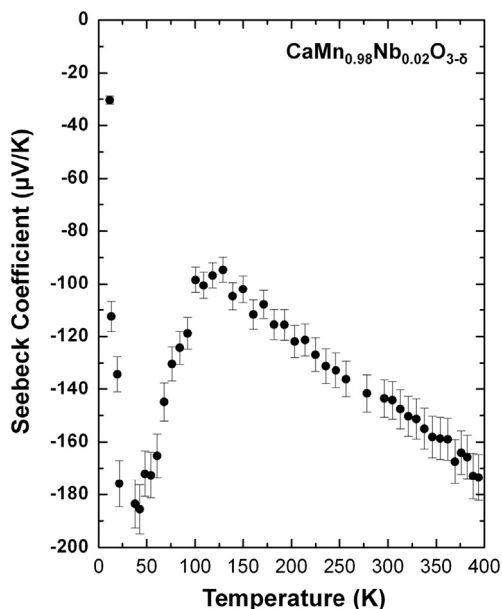
Fig. 7. Temperature dependence of the Seebeck coefficient of the float-zone crystallized material.

Appendix A. Supporting information

Supplementary data associated with this article can be found in the online version at http://dx.doi.org/10.1016/j.jcrysgro.2013.05.020.

References

[1] J. Töpfer, J.B. Goodenough, Journal, of Solid State Chemistry 130 (1997) 117.
[2] L. Rørmark, K. Wiik, S. Stølen, T. Grande, Journal of Materials Chemistry 12 (2002) 1058.
[3] L. Bocher, M.H. Aguirre, R. Robert, D. Logvinovich, S. Bakardjieva, J. Hejtmanek, A. Weidenkaff, Acta Materialia 57 (2009) 5667.
[4] J. Briàtico, B. Alascio, R. Allub, A. Butera, A. Caneiro, M.T. Causa, M. Tovar, Physical Review B 53 (1996) 14020.
[5] W. Kobayashi, I. Terasaki, M. Mikami, R. Funahashi, T. Nomura, T. Katsufuji, Journal of Applied Physics 95 (2004) 6825.
[6] A. Maignan, C. Martin, F. Damay, B. Raveau, J. Hejtmanek, Physical Review B 58 (1998) 2758.
[7] G. Xu, R. Funahashi, Q. Pu, B. Liu, R. Tao, G. Wang, Z. Ding, Solid State Ionics 171 (2004) 147.
[8] D. Alfaruq, E. Otal, M. Aguirre, S. Populoh, A. Weidenkaff, Journal of Materials Research 27 (2011) 985.
[9] M. Miclau, D. Grebille, C. Martin, Journal of Crystal Growth 285 (2005) 661.
[10] P. Reutler, O. Friedt, B. Büchner, M. Braden, A. Revcolevschi, Journal of Crystal Growth 249 (2003) 222.
[11] H. Ohta, S. Kim, Y. Mune, T. Mizoguchi, K. Nomura, S. Ohta, T. Nomura, Y. Nakanishi, Y. Ikuhara, M. Hirano, H. Hosono, K. Koumoto, Nature Materials 6 (2007) 129.
[12] I. Terasaki, Y. Sasago, K. Uchinokura, Physical Review B 56 (1997) R12685.
[13] P. Tomes, M. Trottmann, C. Suter, M.H. Aguirre, A. Steinfeld, P. Haueter, A. Weidenkaff, Materials 3 (2010) 2801.
[14] S. Populoh, M. Trottmann, M.H. Aguire, A. Weidenkaff, Journal of Materials Research 26 (2011) 1947.
[15] P. Tomes, R. Robert, M. Trottmann, L. Bocher, M.H. Aguirre, A. Bitschi, J. Hejtmanek, A. Weidenkaff, Journal of Electronic Materials 39 (2010) 1696.
[16] W. Kobayashi, I. Terasaki, M. Mikami, R. Funahashi, Journal of Applied Physics 95 (2004) 6825.
[17] I. Matsubara, R. Funahashi, T. Takeuchi, S. Sodeoka, T. Shimizu, K. Ueno, Applied Physics Letters 78 (2001) 3627.
[18] L. Bocher, M.H. Aguirre, D. Logvinovich, A. Shkabko, R. Robert, M. Trottmann, A. Weidenkaff, Inorganic Chemistry 47 (2008) 8077.
[19] G. Deng, R. Thiyagarajan, D. Mohan Radheep, E. Pomjakushina, M. Medarde, A. Krzton-Maziopa, S. Wang, S. Arumugam, K. Conder, Journal of Crystal Growth 353 (2012) 25.
[20] S. Ebbinghaus, A. Kalytta, J. Kopf, A. Weidenkaff, A. Reller, Zeitschrift für Kristallographie 220 (2005) 269.
[21] H.S. Horowitz, J.M. Longo, Materials Research Bulletin 13 (1978) 1359–1369.
[22] S.M. Koohpayeh, D. Fort, J.S. Abell, Progress in Crystal Growth and Characterization of Materials 54 (2008) 121.
[23] P.V. Riboud, A. Muan, Journal of the American Ceramic Society 46 (1963) 33.
[24] B.D. White, C.A.M. dos Santos, J.A. Souza, K.J. McClellan, J.J. Neumeier, Journal of Crystal Growth 310 (2008) 3325.
[25] J. Rodriguez-Carvajal, Journal of Physics: Condensed Matter 192 (1993) 55.
[26] J. Laugier, Orient Express (1996).
[27] G.M. Sheldrick, Acta Crystallographica Section A 64 (2008) 112.
[28] L.D. Zhao, B.P. Zhang, W.S. Liu, H.L. Zhang, J.F. Li, Journal of Alloys and Compounds 467 (2009) 91.
[29] K.R. Poeppelmeier, M.E. Leonowicz, J.C. Scanlon, J.M. Longo, W.B. Yelon, Journal of Solid State Chemistry 45 (1982) 71.
[30] B.B. Van Aken, A. Meetsma, Y. Tomioka, Y. Tokura, T.T.M. Palstra, Physical Review B 66 (2002) 224414.
[31] A. Reller, J.M. Thomas, D.A. Jefferson, M.K. Uppal, Proceedings of the Royal Society of London A 394 (1984) 223.
[32] F. Kawashima, X.Y. Huang, K. Hayashi, Y. Miyazaki, T. Kajitani, Journal of Electronic Materials 38 (2009) 1159.
[33] S. Urata, R. Funahashi, T. Mihara, A. Kosuga, S. Sodeoka, T. Tanaka, International Journal of Applied Ceramic Technology 4 (2007) 535.
[34] J.W. Fergus, Journal of the European Ceramic Society 32 (2012) 525.
[35] P.M. Chaikin, G. Beni, Physical Review B 13 (1976) 647.
[36] B. Raveau, Y.M. Zhao, C. Martin, M. Hervieu, A. Maignan, Journal of Solid State Chemistry 149 (2000) 203.
[37] L. Bocher, R. Robert, M.H. Aguirre, S. Malo, S. Hébert, A. Maignan, A. Weidenkaff, Solid State Sciences 10 (2008) 496–501.
[38] M. Miclau, J. Hejtmanek, R. Retoux, K. Knizek, Z. Jirak, R. Frésard, A. Maignan, S. Hébert, M. Hervieu, C. Martin, Chemistry of Materials 19 (2007) 4243.